

# The young star cluster NGC 2362: low-mass population and initial mass function from a *Chandra* X-ray observation<sup>★</sup>

F. Damiani<sup>1</sup>, G. Micela<sup>1</sup>, S. Sciortino<sup>1</sup>, N. Huélamo<sup>2,3</sup>, A. Moitinho<sup>3,4</sup>, F. R. Harnden, Jr.<sup>5</sup>, and S. S. Murray<sup>5</sup>

<sup>1</sup> INAF – Osservatorio Astronomico di Palermo G.S. Vaiana, Piazza del Parlamento 1, 90134 Palermo, Italy

<sup>2</sup> ESO, Casilla 19001, Santiago, Chile

<sup>3</sup> Observatorio Astronomico de Lisboa, Tapada de Ajuda, 1349-018 Lisboa, Portugal

<sup>4</sup> SIM/IDL, Fac. de Ciências da Universidade de Lisboa, Ed. C8 Campo Grande, 1749-016 Lisboa, Portugal

<sup>5</sup> Smithsonian Astrophysical Observatory, 60 Garden St., Cambridge, MA 02138, USA

Received 12 February 2006 / Accepted 9 June 2006

## ABSTRACT

**Context.** We study the stellar population of the very young cluster NGC 2362, using a deep *Chandra* ACIS-I X-ray observation. This cluster, only 5 Myr old, has already cleared most of its inter- and circumstellar dust, and with its small and uniform reddening offers a unique opportunity of studying its pre-main-sequence stellar population with minimal disturbance from a dense interstellar medium.

**Aims.** Our main purposes are to select cluster members down to low masses and to study their properties as a population (spatial properties, initial mass function, and coronal properties).

**Methods.** We compare existing deep optical photometry and H $\alpha$  data with new X-ray data. We use combined optical and X-ray criteria to select cluster members.

**Results.** We detect 387 X-ray sources down to  $\log L_X = 29.0$  (erg/s), and identify most of them (308) with star-like objects. The majority (88%) of optically identified X-ray sources are found to be very good candidate low-mass pre-main-sequence stars, with minimal field-object contamination. This increases the known cluster census by a substantial amount at low masses, with respect to previous optical/IR studies. The fraction of stars with active accretion is found to be in the range 5–9%. We find a significantly wider spatial distribution for low-mass stars than for massive stars (mass segregation). We find only a small spread around the low-mass cluster sequence in the HR diagram, indicating that star formation lasted only about 1–2 Myr. We have derived the cluster initial mass function, which appears to flatten (on the low-mass side) at higher masses with respect to other very young clusters. The quiescent X-ray emission of low-mass cluster stars is found to be rather strictly correlated with the stellar bolometric luminosity: the small spread in this correlation puts an upper bound on the amplitude of X-ray variability on time scales longer than one day (e.g., activity cycles) in such young coronal sources. We find significant X-ray spectral differences between low-mass stars brighter and fainter than  $\log L_X \sim 30.3$  (erg/s), respectively, with X-ray brighter stars showing hotter components ( $kT \sim 2$  keV), absent in fainter stars.

**Key words.** open clusters and associations: individual: NGC 2362 – stars: coroneae – stars: pre-main-sequence – stars: luminosity function, mass function – X-rays: stars

## 1. Introduction

NGC 2362 is a young star cluster that surrounds the O9.5 I star  $\tau$  CMa. This cluster was studied optically by Johnson (1950), Wilner and Lada (1991), Kroupa et al. (1992), Balona & Laney (1996), Moitinho et al. (2001), and most recently by Dahm (2005), who performed a deep H $\alpha$  and IR survey. Moitinho et al. (2001), using deep UBVR photometry, found a distance of 1.5 kpc and an age of 5 Myr. For its age, which is comparable to that of other star-formation regions such as Taurus-Auriga, the cluster is remarkably free of interstellar dust, which means that stars in NGC 2362 have a rather low, uniform reddening, estimated at  $E(B - V) = 0.1$  (Moitinho et al. 2001). The fraction of stars in NGC 2362 showing IR excesses is relatively low (12%, Haisch et al. 2001) compared to clusters of similar age, implying a very low amount of *circumstellar* material, as compared to that commonly found for very young stars in other regions. This peculiarity of NGC 2362 permits a study of the

purely *stellar* properties of very young stars, unbiased by emission/absorption of circumstellar dust and gas. This was shown clearly by Moitinho et al. (2001), who found an exceptionally clean cluster (pre-main-)sequence in the color-magnitude diagram. This fact also permits us to select cluster members with much less field-star contamination than in other young clusters of comparable age.

A preliminary account of this study was presented by Damiani et al. (2005). In this paper we examine the X-ray emission of stars in NGC 2362, first to confirm their membership through X-ray detection, thus establishing a better cluster census, and then to study their spatial distribution, initial mass function, and coronal emission. The excellent spatial resolution of our *Chandra* X-ray data resolves the crowded central cluster region that earlier ROSAT data could not resolve. Our paper is structured as follows: in Sect. 2 we present the X-ray data, while Sect. 3 examines the overall cluster morphology and size. Optical identifications of X-ray sources are presented in Sect. 4, Sect. 5 discusses the X-ray spectra of detected sources and Sect. 6 deals with the dependence of X-ray emission on stellar properties. We compute the cluster initial mass function in Sect. 7, and Sect. 8 concludes with a summary of our results.

<sup>★</sup> Tables 2 and 3 are only available in electronic form at the CDS via anonymous ftp to cdsarc.u-strasbg.fr (130.79.125.5) or via <http://cdsweb.u-strasbg.fr/cgi-bin/qcat?J/A+A/460/133>

## 2. The *Chandra* X-ray observation

We observed NGC 2362 with the *Chandra* X-ray Observatory on December 23-24, 2003, using the ACIS-I imaging spectrometer for an effective exposure time of 97.9 ks. The imaging data (Fig. 1) are characterized by high spatial resolution, with an on-axis point spread function (PSF) *FWHM* of  $\sim 0.5''$ , which allows us to resolve the densest central cluster regions around the O star  $\tau$  CMa, despite the fact that it lies at a relatively large distance of 1.5 kpc. At this distance, the ACIS field of view (FOV – 16.9' on a side) corresponds to  $7.4 \times 7.4$  pc.

We detected 387 point sources in the ACIS image using PWDetect, a wavelet-based detection algorithm developed at INAF-Osservatorio Astronomico di Palermo<sup>1</sup> and already used with success in the analysis of other crowded star clusters (e.g., NGC 6530, Damiani et al. 2004, and more recently, the COUP data on the Orion Trapezium, Getman et al. 2005). Basic features of this algorithm are inherited from its ROSAT predecessor *wdetect* (Damiani et al. 1997a,b). The detection threshold used here was chosen to ensure no more than one spurious detection in the entire ACIS FOV.  $\tau$  CMa itself is the brightest X-ray source (# 199) in the image. Other detected X-ray sources are listed in Table 2.

This cluster was previously observed in X rays with the ROSAT PSPC (Berghöfer & Schmitt 1998; Huélamo et al. 2003), but those data had much lower spatial resolution (PSF wider than  $15''$  on-axis) and sensitivity and only poorly resolved the cluster's X-ray sources (Fig. 2a). However, since the PSPC FOV was much wider ( $2^\circ$  diameter) than the ACIS-I FOV, the ROSAT data are useful for surveying the less dense outer regions of the cluster.

## 3. Cluster size and morphology

The obvious clustering of X-ray sources in the *Chandra* image implies that most X-ray sources are indeed cluster members. This is entirely consistent with expectations, since such very young stars typically emit X rays at a level  $10^3$ – $10^4$  times higher than (older) field stars. Thus X-ray detection is an important membership criterion, which we will use in combination with the optical HR diagram (data from Moitinho et al. 2001, see Sect. 4) to establish a reliable list of members. The nearly circular symmetric distribution of X-ray sources around  $\tau$  CMa implies that we can define a cluster radius from the distribution of X-ray sources. In doing so, we considered only sources detected with more than 20 counts, i.e., detectable across the whole FOV, to compensate for center-to-limb sensitivity variation in the ACIS FOV (mainly due to the strongly varying PSF). The distribution of distances from  $\tau$  CMa (assumed to lie at cluster center) is shown in Fig. 3: the source density falls off rapidly (by a factor of two) from its central peak out to a 2 arcmin radius, and then decreases with a shallower slope to larger radial distances.

The surface density beyond 6 arcmin (2.62 pc, at the cluster distance) is nearly flat, suggesting that this be considered as the “background” value of field X-ray sources. However, a number of considerations argue against this hypothesis: First, the ROSAT image (Fig. 2a) shows a continuing decrease in X-ray source density beyond the limit of the ACIS FOV. Second, the surface density of X-ray sources (above the same threshold), indicated by the horizontal dotted line in Fig. 3, is much lower in another ACIS-I field that was obtained from the archive at a similar angular distance from Galactic center, free of star clusters and

extended emission. This reference field was chosen as *Chandra* ObsId 2787, with 94 ks exposure time, pointed at galactic coordinates  $l = 106.65$ ,  $b = 2.93$ , while NGC 2362 lies at  $l = 238.2$ ,  $b = -5.54$ . These criteria may be somewhat suspect, however: PSPC sensitivity is lower at larger off-axis angles, leading to spurious source density enhancements, and the reference field lies in a different galactic quadrant, in a direction with higher absorption than that toward NGC 2362, which could possibly yield fewer field sources. Another argument can be employed, however, to test whether or not the flattening of surface density in Fig. 3 reflects only the field-object density: at radii beyond 7 arcmin, we find 50 optically-identified X-ray sources (see Sect. 4), of which 36 (72%) fall in the “cluster band” in the HR diagram (see Sect. 4.1). If these were field X-ray sources, we would expect to find them more randomly distributed in the HR diagram, where only 11.4% (773/6777) of all optical stars falls in the cluster band. Thus we predict that only this fraction of the 50 X-ray sources (i.e.,  $\sim 6$  sources) represent interlopers, while about 30 (of 50) sources (i.e., 60%) are cluster members, with a nearly flat distribution out to the edges of the ACIS FOV. We therefore conclude that NGC 2362 has an extended, low-density halo that extends more than 10 arcmin beyond the cluster center. Its outer radius cannot be determined from the ACIS-I data, but the ROSAT data suggest it may be about 15 arcmin, beyond which the PSPC X-ray source density drops markedly. Moreover, if our comparison with the reference field is reliable, the number of field X-ray sources in this latter field (86 sources, in addition to the target itself) is a good estimate of the number of field sources in the NGC 2362 field, leaving about 300 bona-fide X-ray detected cluster members. In Sect. 4.1 below, a slightly lower value (about 270 reliable X-ray members) is obtained from the source positions in the optical HR diagram and in the X-ray color–color diagram.

Upon closer inspection, the centrally-symmetric shape of the cluster is only approximate: at radii less than 4 arcmin, the density is larger South of  $\tau$  CMa than North of it; on larger scales, there are more strong X-ray sources (with  $>200$  counts) to the East (18 sources) than to the West (8 sources). This slight eastern density enhancement coincides with an enhancement in the emission by cool dust at  $60 \mu$ , as observed by the IRAS satellite (Wheelock et al. 1991), and shown in Fig. 2b, where arc-like emission with a radius of about 10 arcmin is nearly centered on  $\tau$  CMa. This is probably due to matter being compressed by the winds of the OB stars in the cluster, on the side closer to the galactic plane (this lies  $5.5^\circ$  towards East-North-East). It is unlikely that the asymmetry arises from differing amounts of line-of-sight absorption toward background objects, since the extinction is uniformly low across the whole cluster, as confirmed with two-color ( $U - B$ ,  $B - V$ ) diagrams obtained from the data of Moitinho et al. (2001). Finally, HR diagram ages of stars in eastern and western regions are not significantly different.

## 4. Optical identifications of X-ray sources

We have cross-identified our X-ray sources with the optical catalog (from data taken at ESO/La Silla Danish 1.5 m) presented by Moitinho et al. (2001), covering essentially our entire ACIS FOV, supplemented by about 1500 additional stars fainter than  $V \sim 21$  from newer VLT/FORS1 photometry (Moitinho et al. 2005), covering only the central  $6.5' \times 6.5'$ . We used a matching distance  $d < 4\sigma_X$  (where  $\sigma_X$  is the PWDetect X-ray position error). In doing this, we found and corrected a systematic offset, between X-ray and optical positions, of  $0.43''$  in RA, and  $-0.07''$

<sup>1</sup> Available at [http://www.astropa.unipa.it/progetti\\_ricerca/PWDetect/](http://www.astropa.unipa.it/progetti_ricerca/PWDetect/)

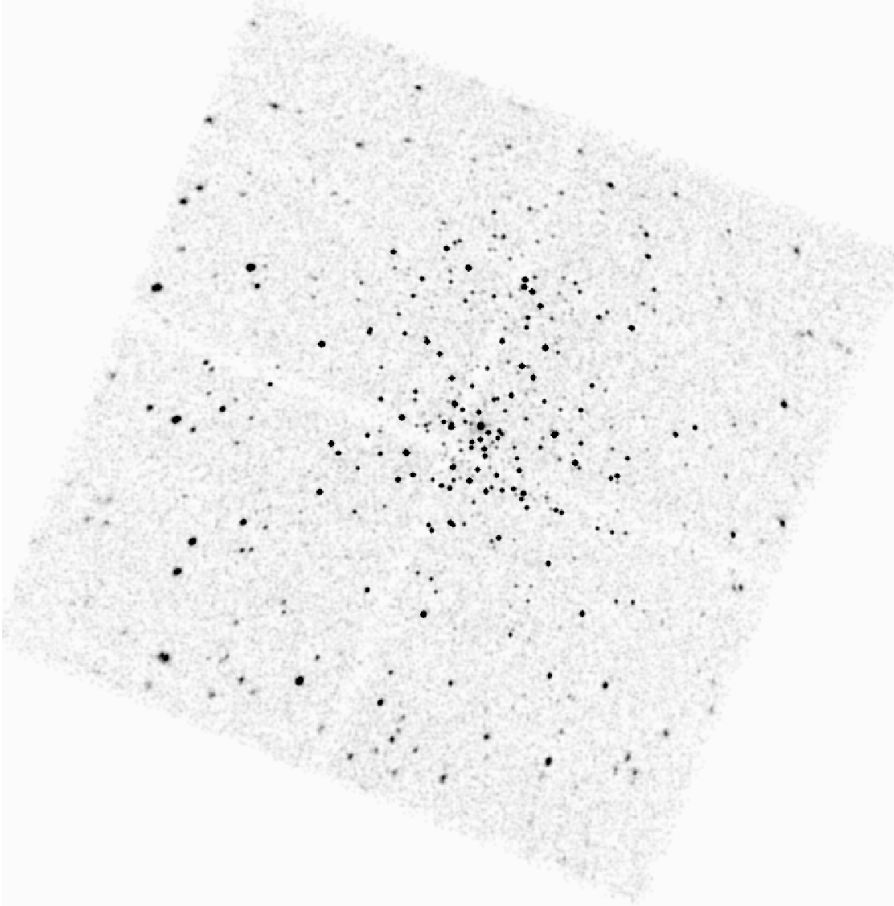


**Fig. 1.** *Chandra* ACIS-I image of NGC 2362, slightly smoothed to emphasize point sources. The field of view is  $16.9' \times 16.9'$ . North is up and East is to the left. 387 point X-ray sources are detected in this image. The brightest X-ray source near cluster center is the massive star  $\tau$  CMa (O9.5 I).

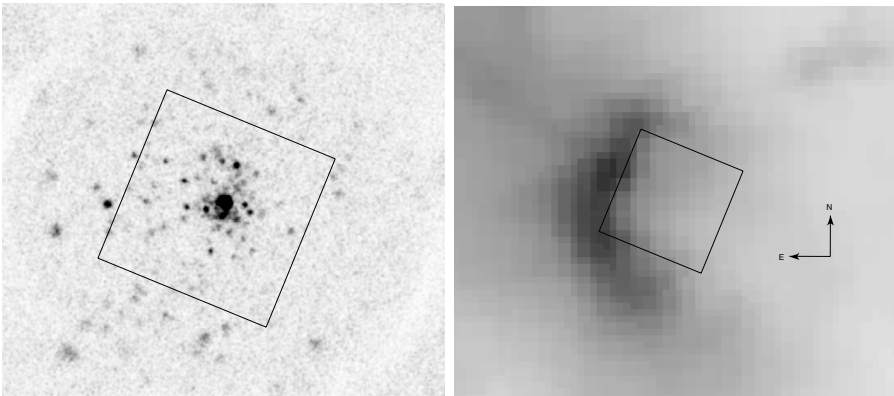


**Fig. 2.** **a)** (left): the ROSAT PSPC image of NGC 2362, of much lower spatial resolution than the *Chandra* ACIS-I image. **b)** (right): IRAS  $60\mu$  image of the surroundings of NGC 2362, showing an arc-like enhanced emission around the eastern part of the cluster. In both images, North is up and East is to the left, and the square outlines the *Chandra* ACIS-I FOV of Fig. 1.

in Declination. The agreement between X-ray and optical positions is very good (see Table 3): for 308 X-ray sources identified with an optical counterpart, we find only 7 double identifications. 79 X-ray sources remained optically unidentified.

Considering the surface density of optical and X-ray objects, and the mean identification radius, we obtain an estimate of 89 expected spurious identifications between these two catalogues, under the (incorrect) assumption of no correlation between them. Taking this correlation properly into account (as described by Damiani et al. 2006), we obtain the much smaller number of 22 predicted spurious matches, randomly distributed among optical stars.

Moreover, we have cross-identified our X-ray sources (using the same matching criterion) with the list of 130  $H\alpha$ -emission stars from Dahm (2005) that fall in a  $11' \times 11'$  region centered on  $\tau$  CMa (thus fully within our ACIS FOV). Among the  $H\alpha$

emitters, 91 are identified with X-ray sources (with no double identifications), and 39 are without X-ray counterparts (Table 3).

A  $(V, V - I)$  diagram of the NGC 2362 ACIS field is presented in Fig. 4, with X-ray sources indicated by large dots, and  $H\alpha$  emission stars, by plus signs. Evolutionary tracks, isochrones and the ZAMS from Siess et al. (2000), all appropriately reddened, are also shown. The majority of X-ray sources (about 270, or 88% of those identified) fall around the NGC 2362 sequence and comprise both massive OB stars on the main sequence and low-mass stars in their pre-main-sequence (PMS) band. As already noted, e.g., by Moitinho et al. (2001) or Dahm (2005), this is quite narrow and separated from the field, permitting easy selection of members as compared with other clusters containing PMS stars. X-ray detected stars are mostly found in this band, at least down to  $V \leq 20$ , corresponding to a  $\sim 0.35 M_{\odot}$

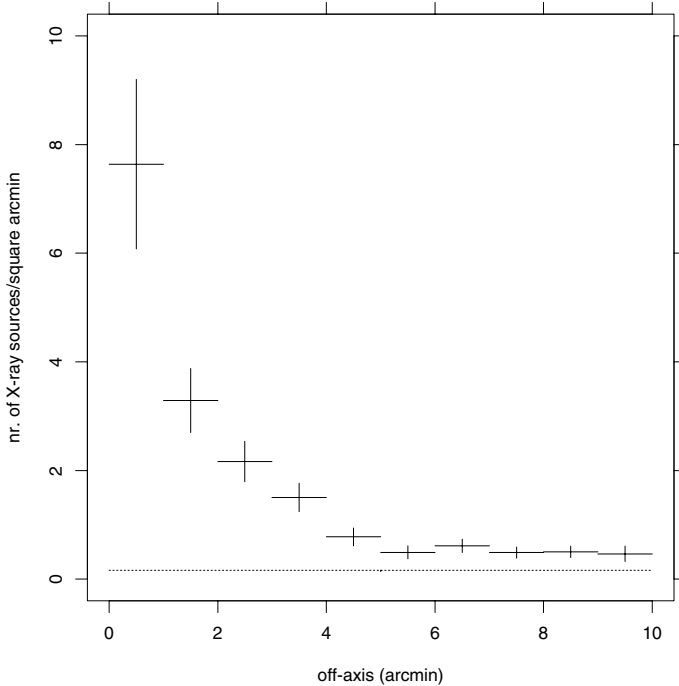


**Fig. 3.** Surface density of X-ray sources (detected with more than 20 X-ray counts in the ACIS FOV) as a function of distance from  $\tau$  CMa, assumed to lie at cluster center. The dotted horizontal line is the average surface density of a reference galactic-plane field with the same exposure time as the NGC 2362 field.

star, while at fainter magnitudes X-ray detection becomes increasingly more rare. The faintest X-ray detected object along the cluster band has  $V \sim 23$  (slightly less than  $0.2 M_{\odot}$ ). With the ACIS FOV containing 6777 stars throughout the HR diagram, we find 773 stars in and around this cluster band and estimate that the cluster band contains this same fraction of spurious X-ray/optical identifications, namely only 2.5 objects. The remainder of the predicted  $\sim 22$  spurious matches presumably lie elsewhere in the diagram.

H $\alpha$ -emission stars not detected in X rays are also found preferentially at  $V > 20$  (the brightest one has  $V = 18.9$ ), which we interpret as due to the sensitivity limit of our X-ray observation, not evidence for a separate class of objects.

The fact that our photometry along the cluster band appears to reach deeper than the X-ray sensitivity limit raises the question of what these optically-unidentified X-ray sources really are. Only a dozen of them are located around cluster center and might be missed in our optical catalog because they fall in the halos of visually bright stars. These are likely low mass cluster members. The bulk of unidentified X-ray sources, however, are not likely to be still lower-mass cluster stars, since our optical catalog encompasses them, down to the substellar limit with the VLT data (these cover only the central part of the ACIS FOV, but there is no difference in the spatial density of unidentified X-ray sources inside and outside the VLT field). We therefore suspect they may be faint, unrelated objects, with large X-ray/visual flux ratios. This is plausible, since their spatial distribution is rather flat, and their number (79) is close to the number of field X-ray sources (86) in our reference field.

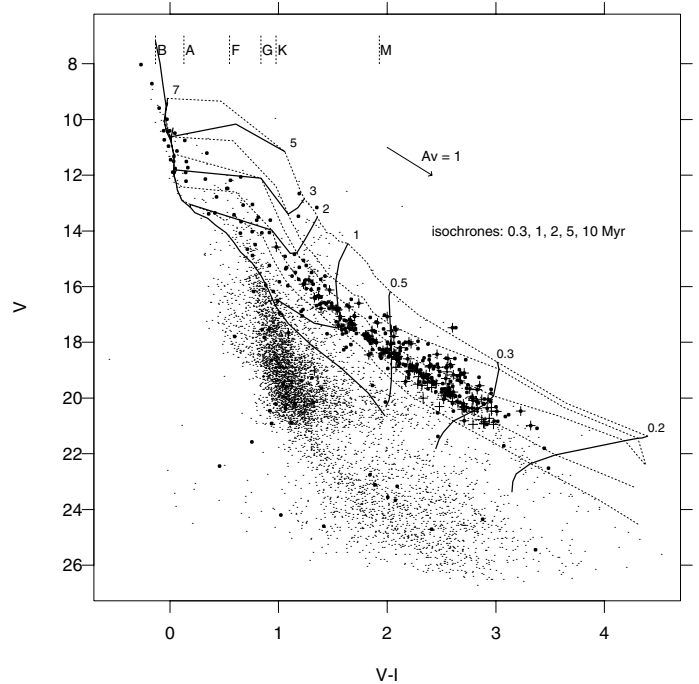


**Fig. 4.** ( $V, V - I$ ) color-magnitude diagram of all objects in the ACIS FOV, with photometry from Moitinho et al. (2001; data taken at ESO/La Silla Danish 1.5 m), and new VLT data for  $V > 21$ . Filled dots are X-ray sources; plus signs mark positions of H $\alpha$  emission stars from Dahm (2005). Evolutionary tracks (thick lines) for star masses between 0.2 and 7 solar masses, as indicated, are from Siess et al. (2000), as are the ZAMS for  $V > 10$  (thick line) and isochrones (dotted lines). The upper ZAMS is from Schmidt-Kaler (1982). Note that the VLT data cover a smaller field than the Danish 1.5 m data, hence the change in appearance of the diagram around  $V \sim 21$ .

#### 4.1. Member selection

In the HR diagram, we expect essentially no field stars in the ACIS FOV brighter than  $V = 12$ . All stars brighter than this limit (58 objects with spectral types earlier than A, including the O star  $\tau$  CMa) are therefore very probable cluster members<sup>2</sup>. For lower-mass stars, our member selection is based on X-ray detection *and colors*, as well as position in the HR diagram. We have defined five groups in the HR diagram comprising most cluster stars (Fig. 5): group #1 contains O to early A stars, group #2 contains mid-A to G stars, and group #3 is defined as a narrow ( $\Delta V = 0.6$  mag) strip where the densest concentration of X-ray sources is found<sup>3</sup>, with colors of early K to mid-M stars. Above the group #3 strip we assign possible cluster binaries (or younger members?) falling in a wider strip ( $\Delta V = 1.2$  mag) to group #4, while a residual, more sparse population in a strip with  $\Delta V = 0.9$  mag below group #3 is assigned to group #5. Groups #1 to 5 contain respectively 22, 23, 128, 66, and 32 X-ray sources, in total, 271 of the 308 optically identified sources. The 37 remaining optical identifications are more scattered in the HR diagram and almost certainly do not belong to the cluster; these we classify as group #6. Group #7 comprises

<sup>2</sup> Our sample includes brighter, SIMBAD database stars that were missed due to saturation in the Moitinho et al. (2001) catalog.

<sup>3</sup> The position and width of this strip in the HR diagram were derived directly from the data, to avoid all uncertainties possibly arising from the adoption of a particular set of PMS evolutionary tracks.

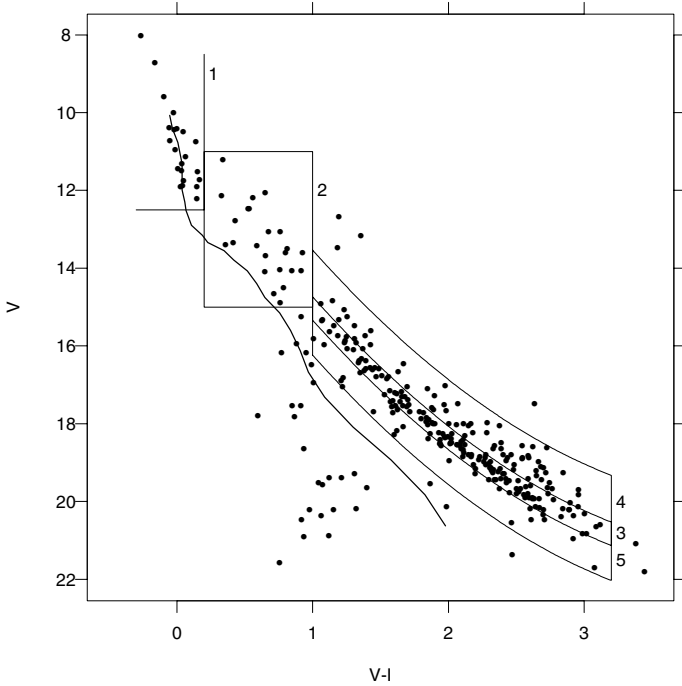


**Fig. 5.** ( $V, V - I$ ) diagram of X-ray detected sources down to  $V = 22$ , with the definition of the five groups discussed in the text (numbered 1–5).

the optically unidentified X-ray sources (non-members too, as discussed above).

Using the ACIS detector’s spectral resolution, we have also studied the spectral properties of the NGC 2362 sources, as discussed in Sect. 5. Here we define X-ray hardness ratios (equivalent to X-ray colors) as a useful means of studying broadband X-ray colors of our cluster stars in order to confirm cluster membership. We define these hardness ratios as  $HR1 = (M - S)/(M + S)$ , and  $HR2 = (H - M)/(H + M)$ , where  $S$ ,  $M$ , and  $H$  are the source X-ray counts in the soft (0.3–1.2 keV), medium (1.2–2.2 keV), and hard (2.2–8.0 keV) bands, respectively. High values of HR1 and HR2 correspond generally to harder (hotter) X-ray emission, and HR1 also increases for high absorption. These hardness ratios are reported in Table 2. Figure 6 shows the distributions of data points in the ( $HR1, HR2$ ) plane for sources in groups #1–7 defined above. Only sources with more than 20 detected counts are shown, but similar trends are observed for fainter sources. We observe that massive stars in groups #1–2 (panel a) have hardness ratios similar to those of low-mass cluster stars in groups #3–5 (panel b), suggesting that emission from cluster B and A stars may be due to unknown lower-mass companions. In panel b, cluster stars that exhibited X-ray flares (crosses) in our observation show X-ray emission only moderately harder than non-variable stars. In contrast, objects in groups #6–7, which we regard as not belonging to the cluster, have a very different distribution of HR1 and HR2, with larger average values of both indices. A good demarcation between cluster and non-cluster sources appears to be the line  $HR1 + HR2 = 0$  (shown in the figure): sources with  $HR1 + HR2 > 0$  are very unlikely to belong to the cluster. To confirm this, we have marked with large circles in Fig. 6 X-ray sources whose X-ray spectra show high absorption and high-energy tails (well fitted by power-law models, see Sect. 5). These are good AGN candidates: all of them fall in the region  $HR1 + HR2 > 0$ , and none of them is found among sources in

groups #1–5, which should thus constitute a very “clean” sample of cluster X-ray sources.

#### 4.2. Space distribution, stellar ages, and mass segregation

Because the spatial distributions of the different groups we have defined may give further clues about their nature, we show cumulative off-axis angle distributions of the sources from groups #1–5 in Fig. 7, together with sources having  $HR1 + HR2 > 0$ . These latter sources are distributed as a (concave-downward) parabola, corresponding to a flat distribution, as expected for field stars or AGNs. A Kolmogorov-Smirnov (K-S) test gives a probability of  $P_0 = 13\%$  that the distribution of these objects is indistinguishable from a flat distribution. In contrast, cluster sources have very different, centrally-peaked distributions. Apart from the massive stars in group #1, sources in group #3 (thick solid line in Fig. 7), are found in a very narrow region of the HR diagram and are certainly least contaminated by non-members. The probability that their distribution is indistinguishable from sources with  $HR1 + HR2 > 0$  is very low,  $P_0 = 1.1 \times 10^{-8}$ . The possible contamination for groups #2, #4 and #5 can be estimated from their respective distributions: in fact, their properties are closer to that of group #3 than to that of field objects (the K-S test gives probabilities of being indistinguishable from group #3 of  $P_0 = 82\%$ ,  $9\%$ , and  $56\%$ , respectively). The degree of contamination is thus also very low, like that of group #3. We therefore arrive at the conclusion that X-ray sources in the relatively scattered regions (in the HR diagram) of groups #2, #4, and #5 have nearly the same probability of being cluster members as sources in the narrow region of group #3.

The observed small spread around the cluster sequence can be in part attributed to binaries and in part may be due to a small (1–2 Myr) spread in stellar ages (in agreement with Moitinho et al. 2001). It is unlikely that the  $V - I$  colors are affected by non-stellar excesses (e.g. veiling), usually attributed to circumstellar accretion, because accretion has virtually ceased in NGC 2362<sup>4</sup>.

Using our data, we have also investigated whether accretion-induced UV excesses can be observed for our X-ray sources. Figure 8 shows a ( $U - B, B - V$ ) color-color diagram for objects in the ACIS FOV: it is clear that reddening is very uniform across the cluster, but at least ten PMS candidate members (i.e., X-ray sources in groups #3–5) deviate from reddened ZAMS colors. This is incompatible with even-higher reddening and normal colors but suggestive of an excess in the  $U$  band, which in PMS stars is typically caused by active accretion on the star. The fact that most cluster stars with a strong  $U - B$  excess in Fig. 8 also have  $H\alpha$  emission (large empty circles) may also be evidence of accretion. These UV-excess stars are only 3–4% of the total X-ray selected cluster population: all other stars do not exhibit strong UV excesses and are therefore also not expected to show  $V$ -band excess.

Moreover, if we assume that all cluster stars are reddened by the average cluster  $A_v$ , then we find 22 members showing a  $U - B$  excess<sup>5</sup> (at  $3\sigma$  and by more than 0.4 mag), most of which fall in groups #3 (9 stars, or 7% of total), #4 (8 stars, or 12%), and #5 (1 star, or 3%). Thus we see that there is an increase in the percentage of stars with UV excess in going upwards across

<sup>4</sup> The fraction of accreting stars was estimated by Dahm (2005) to be 5–9%, and our data suggest an even lower fraction.

<sup>5</sup> For stars without reliable cluster membership information this criterion cannot be used because the ( $U - B, B - V$ ) colors of heavily reddened background (super)giants may mimic those of cluster stars with a  $U - B$  excess.

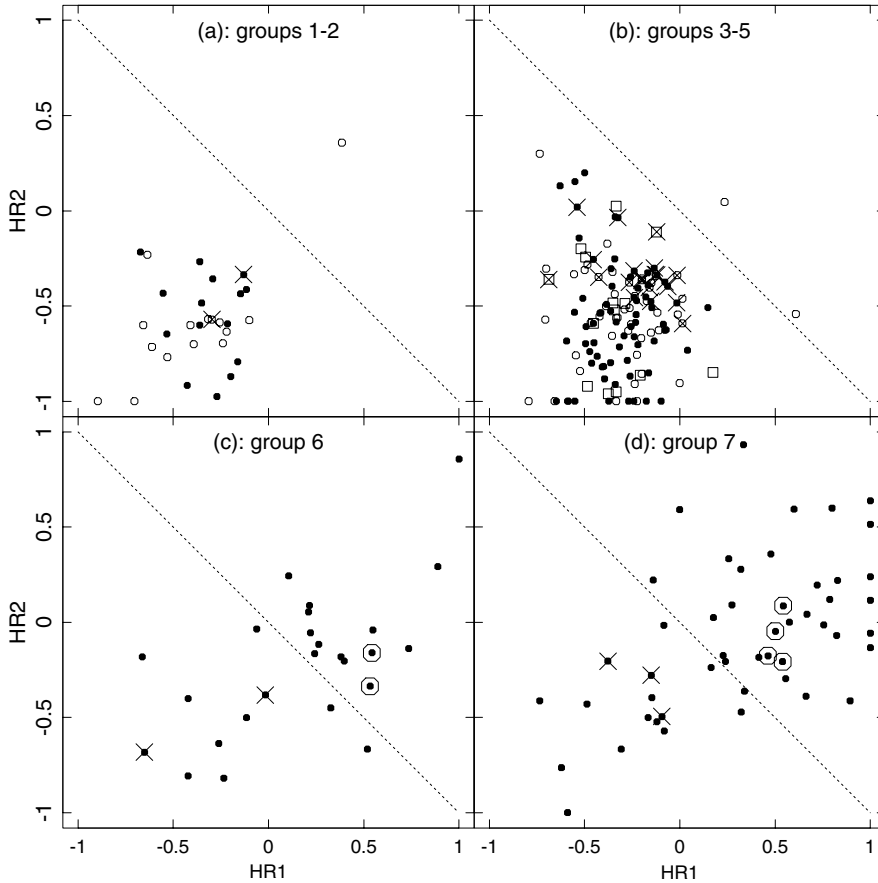


**Fig. 6.** ( $HR1$ ,  $HR2$ ) diagrams for X-ray sources in groups #1-7. Panel **a**): group #1 (filled dots) and group #2 (empty dots); panel **b**): group #3 (filled dots), group #4 (empty dots), and group #5 (empty squares); **c**): group #6, non-cluster members; and **d**): group #7, unidentified X-ray sources. In all panels, crosses are sources showing X-ray flares, and large circles are sources whose X-ray spectra show large absorption and high-energy tails. The dotted lines demarcate the region  $HR1 + HR2 < 0$ , where nearly all cluster members are found.

the cluster sequence in the HR diagram, from group #5 to #3 to #4. Since UV excesses are usually more common among the youngest PMS stars, also expected to lie higher in the HR diagram, this upward increase also suggests that the width of the cluster sequence is related at least in part to some age spread and not only to binarity and/or photometry error effects.

In principle, the cluster age spread might be derived by examining the main-sequence turn-on in Fig. 4. This, however, is poorly defined in our (mostly group #2 star) data: the ZAMS becomes noticeably less populated at  $V > 12$ , suggesting the same age as for low-mass PMS stars, but there are a few stars falling close to the ZAMS still at  $V \sim 14$ . If these are cluster members, they would be nearly 10 Myr old, thus implying a much larger age spread than suggested above. However, such a relatively large spread in the HR diagram may partially arise from field-star contamination, and lacking other membership indications (e.g., Lithium abundance or radial velocity) for individual stars, we cannot firmly establish the existence of such a large age spread. Similarly, the few group #5 stars closer to the 10 Myr than to the 5 Myr isochrone in Fig. 4 might either be field stars or cluster fast rotators (looking bluer because of von Zeipel effect). This prevents us from reliably inferring a large age spread for NGC 2362.

The lowest spatial distribution curve of Fig. 7 deserves a separate discussion. These group #1 massive stars appear to be much more centrally-peaked than the distributions of less massive stars in groups #2-5<sup>6</sup>. This fact is confirmed if we add to group #1 stars the 38 massive stars that are not detected

in X-rays, but which are very probable cluster members (on the basis that they cluster around  $\tau$  CMa). It therefore appears that there is genuine mass segregation in NGC 2362, with massive stars being significantly more concentrated than less-massive cluster stars. With the evaporation time estimated by Dahm (2005) to be  $\geq 30$  times the present cluster age, it is unlikely that this segregation was caused by dynamical evolution; it might rather have originated in the epoch when the stars of NGC 2362 were forming. This implication is similar to that found by Raboud & Mermilliod (1998) and Raboud (1999) in the very young cluster NGC 6231, and by Dolan & Mathieu (2001, 2002) in the  $\lambda$  Ori cluster. Littlefair et al. (2003) also found evidence of primordial mass segregation in the older cluster NGC 2547.

## 5. X-ray luminosities and spectra

### 5.1. Quiescent and flaring emission

Since low-mass stars often exhibit impulsive flares superimposed on relatively steady, or “quiescent” X-ray emission, we tested all X-ray sources for variability. Forty-eight of 387 sources are found to be variable with more than 99% confidence, according to a K-S test. The probability  $P_{K-S}$  that a source is not variable is reported in Table 2. Not all variable sources are flaring, however: a number of them apparently undergo slow variations, either brightening or fading, which can be empirically modeled as constant count-rate gradients (during our observation).

For 29 sources the empirical models failed (with confidence  $>80\%$ ), and inspection of their X-ray light curves showed

<sup>6</sup> The K-S test gives a probability of only  $P_0 = 0.2\%$  that group #1 is indistinguishable from group #3).

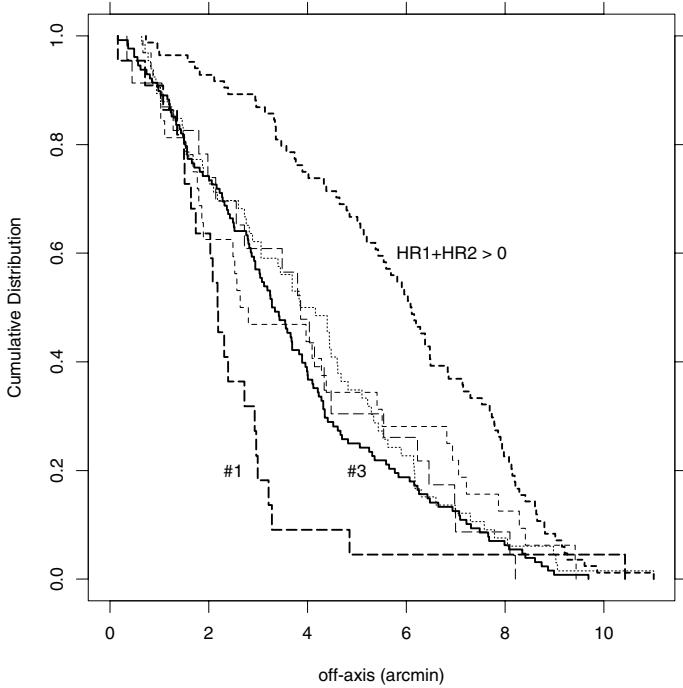


**Fig. 7.** Cumulative distributions of off-axis distances for sources in groups #1 (thick dashed line), #2 (thin dashed line), #3 (thick solid line), #4 (thin dotted line), #5 (thin short-dashed line), and sources with  $HR1 + HR2 > 0$  (thick short-dashed line). Distributions for groups #1 and #3, and for the group with  $HR1 + HR2 > 0$  are labeled.

instead classical, impulsive stellar flares. Most (22) of these occurred in stars belonging to groups #3–5, i.e., to cluster candidate late-type PMS stars. Five “flaring” sources are field objects (in groups #6–7).

All flaring sources were modeled as a constant count rate plus an impulsive rise with exponential decay, and the best model parameters (quiescent count rate, peak rate and time, and decay time) were found by non-linear fitting routines. This allowed us to assign a quiescent count rate to these sources (also reported in Table 2), which we will use in the following analysis for such flaring sources, instead of the average count rate. This permits a more meaningful comparison with non-flaring sources. A more detailed analysis of X-ray variability properties of NGC 2362 sources is deferred to a future work.

## 5.2. X-ray spectra across the HR diagram

Since the ACIS detector has moderate energy resolution, we have attempted to fit (using XSPEC V11.3) the X-ray spectra of our sources to infer coronal properties. In a customary manner, we have chosen *apec* thermal models with the absorption fixed (differential reddening appears absent) at  $N_H = 6.88 \times 10^{20} \text{ cm}^{-2}$ , corresponding to the cluster optical extinction.

For convenience, we categorized our X-ray sources as “strong” (more than 100 ACIS counts) or “weak” (less than 100 counts). With the conversion factor to be derived below, this separation lies at  $\log L_X \sim 30.3$  (erg/s). Spectral fitting was attempted individually only for “strong” sources. The strongest source, O star  $\tau$  CMa, has a significantly softer spectrum (typical of O stars) than all other sources; moreover, with a count rate of  $8.06 \times 10^{-2}$  cts/s, it is probably affected by photon pile-up, making reliable spectral fitting difficult. Since we are focusing

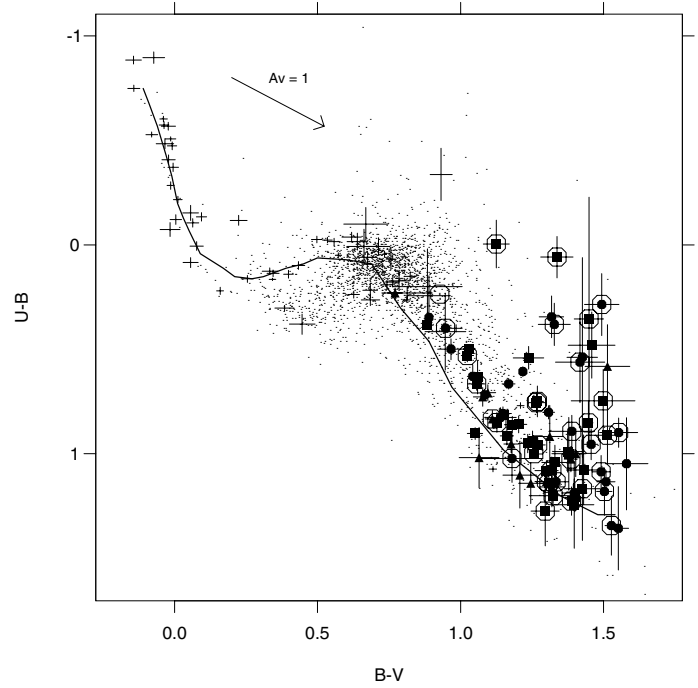


**Fig. 8.** The  $(U - B, B - V)$  color-color diagram for all objects in the ACIS FOV (small dots). Also shown are the ZAMS and the reddening vector. X-ray sources are indicated with errors bars: those of group #3 are indicated with filled squares, those of group #4, with filled circles, and those of group #5 with filled triangles. Large empty circles denote stars with  $H\alpha$  emission.

on properties of lower-mass stars, we have not considered this source in this analysis.

The X-ray spectra of most sources are well fit by one- or two-temperature models. However, the derived fitting parameters are affected by large errors (most sources are not far above the 100-count threshold), and more importantly we could not identify any sensible trends of these parameters<sup>7</sup> with other stellar parameters such as optical colors and luminosities, age, or mass. We therefore do not consider these individual fits to be particularly meaningful.

As an alternative approach, we fitted the combined (summed) X-ray spectra of *groups* of X-ray sources, with suitable weighted-average response matrices computed using the capabilities of the CIAO 3.2 (and later versions) analysis software (in particular, tasks *mkwarf* and *mkrmf*). We combined all spectra of “strong” and “weak” sources, respectively, belonging to each of groups #1–5, excluding flaring X-ray sources in order to study only the quiescent spectral properties. This approach benefits from the use of spectra with much larger number of counts than in the individual spectra and also enables a study of the average spectral properties of weaker sources that cannot be studied individually.

Instead of allowing the temperature of individual thermal components to vary, we have chosen a three-temperature model with *fixed* temperatures  $kT_1 = 0.5$  keV,  $kT_2 = 1.0$  keV, and  $kT_3 = 2.0$  keV and derived the corresponding emission measures as fitted parameters<sup>8</sup>. This approach is qualitatively similar

<sup>7</sup> E.g., cooler  $kT_1$  or hotter  $kT_2$  temperatures, emission measures  $EM_1$  or  $EM_2$ , or emission-measure ratio  $EM_1/EM_2$ .

<sup>8</sup> With the available count statistics, attempting to derive individual temperatures does not constrain the fitted values; hence the necessity of our approach.



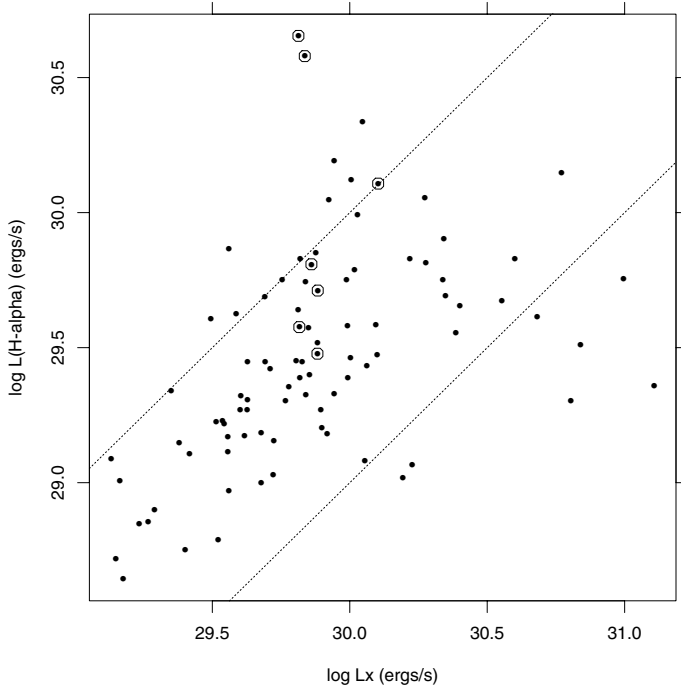


**Fig. 9.** Plot of  $H\alpha$  luminosity  $L_{H\alpha}$  vs. X-ray luminosity  $L_X$ . Large circles are stars with  $EW(H\alpha) > 10 \text{ \AA}$ . The two dotted lines indicate loci where  $L_{H\alpha} = L_X$  and  $L_{H\alpha} = 0.1L_X$ , respectively.

to a reconstruction of the differential emission-measure distribution over a range of temperatures, as has been done for other PMS stars at higher spectral resolution (see e.g., Argiroffi et al. 2005, and references therein), but our limited resolution and total counts force us to use coarse temperature bins. The temperatures chosen here span the range usually found for PMS stars in those more detailed studies.

Our results are summarized in Table 1: the good reduced  $\chi^2$  values indicate that this approach provides a reasonable representation of our sources' X-ray spectra and permits us to discern some patterns: strong sources in all groups tend to have rather flat emission-measure distributions, with  $EM_1 \sim EM_2 \sim EM_3$ , while weak sources show in almost all groups a drop in the emission measure ratio  $EM_3/EM_2$  at the highest temperatures, i.e., at  $kT \sim 2 \text{ keV}$ . Although the number of counts in each summed spectrum is much larger than for individual spectra, the errors on fitted parameters are still relatively large and prevent finding significant systematic differences in emission measure distributions among strong (weak) sources belonging to different groups. The lack of X-ray spectral difference between stars in group #1 and groups #3–5, which have very different mass and structure, is again suggestive that the former X-ray sources are actually due to lower-mass companions rather than to the massive stars themselves, as suggested in section 4.1 above.

To convert X-ray count rates to fluxes for cluster stars, conversion factors were derived by adopting absorbed thermal models with three temperatures for strong sources, or two temperatures for weak sources<sup>9</sup>. According to the results above, we assumed the two coolest components to be at (fixed) temperatures  $kT_1 = 0.5 \text{ keV}$  and  $kT_2 = 1.0 \text{ keV}$  for both weak and strong sources, while adding a hotter component at  $kT_3 = 2.0 \text{ keV}$  only for strong sources. The emission measure values were

<sup>9</sup> For weak sources, the emission measure at the highest temperature is very low and can be considered negligible.

assumed to be the same,  $EM_1 = EM_2 (= EM_3)$  for all two (three) components. The resulting conversion factors are  $6.564 \times 10^{-12} \text{ erg cm}^{-2} \text{ count}^{-1}$  and  $10.16 \times 10^{-12} \text{ erg cm}^{-2} \text{ count}^{-1}$ , respectively for weak and strong sources. The weakest detected sources have  $\log L_X = 29.0 \text{ (erg/s)}$ .

Six strong X-ray sources (numbers 286, 351, 371, 375, 377, and 378 in Table 2, all falling in groups #6–7, and thus not included in “combined” spectra of Table 1) have stronger low-energy cutoffs, indicative of large absorption, and high-energy tails, better fitted with absorbed power-laws than with multi-temperature thermal models. This makes them better candidates of AGNs than of stellar sources.

## 6. Properties of X-ray emission of NGC 2362 stars

We have examined the relationship between the X-ray emission of NGC 2362 stars and their  $H\alpha$  emission, as reported by Dahm (2005). Rather than line equivalent widths (EW), we consider line luminosities and compare them to our X-ray luminosities.  $H\alpha$  fluxes were derived from the equivalent widths and  $R$ -band fluxes given by Dahm (2005) and the prescription given by Reid et al. (1995). Figure 9 is a plot of  $H\alpha$  luminosity  $L_{H\alpha}$  vs. X-ray luminosity  $L_X$ . We note the existence of a correlation between these two quantities, which scale approximately as  $L_{H\alpha} = 0.3L_X$ ; most cluster stars are found between the loci  $L_{H\alpha} = L_X$  and  $L_{H\alpha} = 0.1L_X$ , respectively. This suggests that the  $H\alpha$  emission of most stars in NGC 2362 has a chromospheric origin, in agreement with Dahm (2005), and scales in proportion to the (coronal) X-ray emission. Stars with  $EW(H\alpha) > 10 \text{ \AA}$  (the usual definition of classical T Tauri stars, or CTTS) can reach the highest values of  $L_{H\alpha}$  in NGC 2362, which are still much lower than  $L_{H\alpha}$  of PMS stars, e.g., in the Taurus-Auriga region, where, despite the fact that NGC 2362 is richer than Tau-Aur, it rises above  $L_{H\alpha} = 10^{32} \text{ erg/s}$ . The correlation between  $L_X$  and  $L_{H\alpha}$  in NGC 2362 appears to break down for stars with  $L_X \geq 30.5 \text{ erg/s}$ , where the  $H\alpha$  luminosity is no longer proportional to the very high X-ray luminosity, but remains  $L_{H\alpha} \leq 10^{30.2} \text{ erg/s}$ . An analogous plot to Fig. 9 was reported for Taurus-Auriga by Damiani & Micela (1995), where the same correlation was found for weak-line T Tauri stars (WTTS), but not for CTTS. With that sample (and Tau-Aur in general) not as rich as that of NGC 2362, the region of  $L_X > 30.5 \text{ erg/s}$  in Tau-Aur is almost unpopulated.

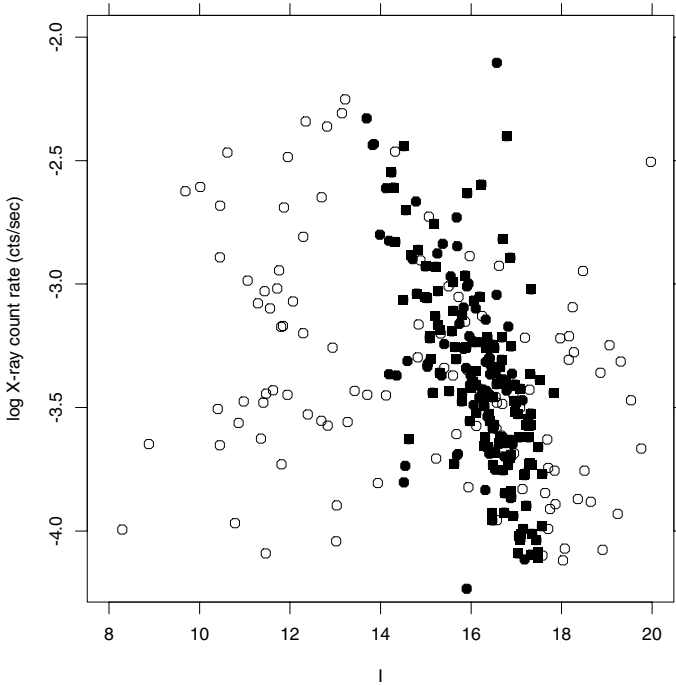
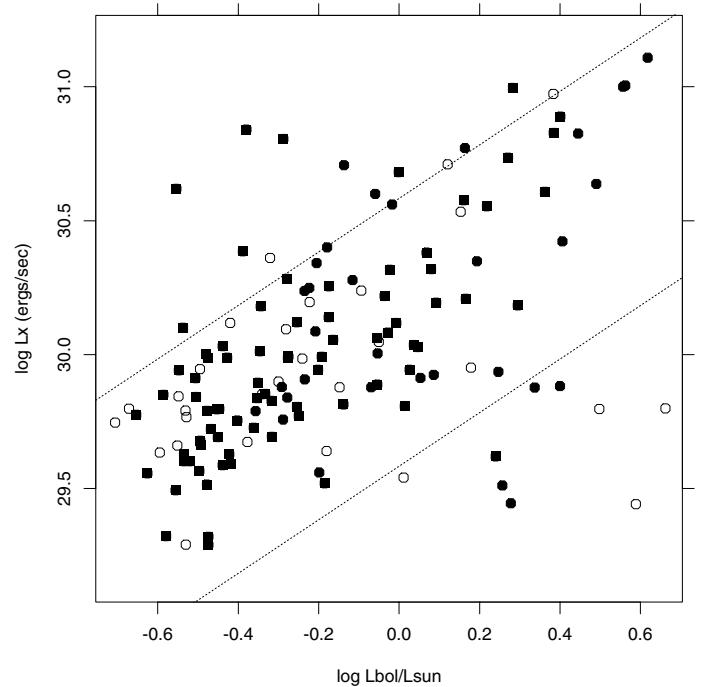
Figure 10 compares quiescent count rates for all X-ray sources in the NGC 2362 field with their  $I$  magnitude. A good correlation, spanning 4 magnitudes in  $I$  and almost two orders of magnitude in X-ray count rate with very few outliers, is found for stars in groups #3–4 (filled symbols). If all low-mass PMS stars in the cluster follow this correlation (i.e., if there is no other population of much fainter X-ray emitters in the same  $I$  magnitude range), then we can infer something about the completeness of our sample of X-ray selected members. In particular, the average correlation of Fig. 10 starts crossing our average detection threshold ( $\log \text{count-rate} \sim -4.2 \text{ counts/s}$ ) at  $I \geq 17$ . At the cluster age this corresponds to  $V \geq 19$ , suggesting that essentially all PMS cluster stars brighter than this limit have been detected in our X-ray observation. This magnitude limit agrees well with that found in Sect. 4; beyond this, we start to miss  $H\alpha$  emission stars as X-ray sources. Therefore, we are likely to have selected a *complete* sample of NGC 2362 members down to this limit, which corresponds to about  $0.4 M_\odot$ .

Figure 10 suggests that the X-ray luminosity  $L_X$  of PMS cluster stars is well correlated with their bolometric luminosity  $L_{\text{bol}}$ , not unlike the case in other star-forming regions. With  $L_{\text{bol}}$  as derived from the tracks of Siess et al. (2000), using the



**Table 1.** Average emission measure distributions for NGC 2362 stars.

Non-flaring strong sources (>100 X-ray counts)						
group #	Nr. sources	Total counts	$\chi^2/\text{d.o.f.}$	Emission measure ( $10^{53} \text{ cm}^{-3}$ )		
				$kT = 0.5 \text{ keV}$	$kT = 1.0 \text{ keV}$	$kT = 2.0 \text{ keV}$
1	4	767	68.64/67	$4.27 \pm 1.72$	$2.76 \pm 2.04$	$2.32 \pm 1.12$
2	5	1518	100.43/106	$6.41 \pm 2.09$	$6.87 \pm 2.27$	$3.92 \pm 1.23$
3	9	1395	107.12/108	$2.48 \pm 1.10$	$2.54 \pm 1.27$	$3.01 \pm 0.721$
4	7	1446	107.10/104	$5.10 \pm 1.53$	$3.73 \pm 1.69$	$2.82 \pm 0.904$
5	1	104	10.21/11	$3.27 \pm 2.97$	$2.21 \pm 3.77$	$0.658 \pm 2.45$
Non-flaring weak sources (<100 X-ray counts)						
group #	Nr. sources	Total counts	$\chi^2/\text{d.o.f.}$	Emission measure ( $10^{53} \text{ cm}^{-3}$ )		
				$kT = 0.5 \text{ keV}$	$kT = 1.0 \text{ keV}$	$kT = 2.0 \text{ keV}$
1	16	742	44.29/68	$1.40 \pm 0.461$	$0.751 \pm 0.487$	$0.431 \pm 0.257$
2	15	352	25.30/35	$1.62 \pm 0.414$	$0.107 \pm 0.396$	$3.41 \times 10^{-15} \pm 0.196$
3	105	2769	169.91/158	$0.647 \pm 0.144$	$0.829 \pm 0.16$	$0.0291 \pm 0.0904$
4	46	1490	109.48/116	$0.913 \pm 0.255$	$0.792 \pm 0.28$	$0.169 \pm 0.155$
5	28	645	84.05/73	$0.522 \pm 0.269$	$0.758 \pm 0.315$	$1.96 \times 10^{-13} \pm 0.177$

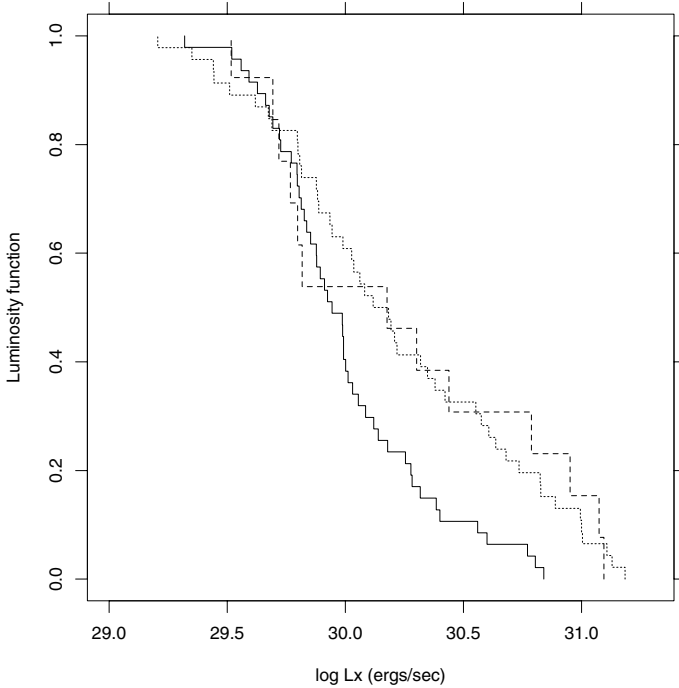
**Fig. 10.** Quiescent X-ray count rate vs.  $I$  magnitude, for all X-ray detected objects in the NGC 2362 field. Filled squares are stars in group #3 and filled circles are stars in group #4.**Fig. 11.** Quiescent X-ray luminosity  $L_X$  vs. stellar bolometric luminosity  $L_{\text{bol}}$ , for X-ray detected candidate PMS stars in NGC 2362. Symbols same as in Fig. 10. The two dotted lines correspond to  $L_X = 10^{-3} L_{\text{bol}}$  and  $L_X = 10^{-4} L_{\text{bol}}$ .

color transformation of Kenyon & Hartmann (1995), Fig. 11 shows that this is indeed the case: most PMS cluster stars (excluding massive stars) have  $L_X$  lying in a well-defined band between  $10^{-3} L_{\text{bol}}$  and  $10^{-4} L_{\text{bol}}$ . Filled symbols of the figure indicate group #3 (squares) and group #4 (circles) stars. The correlation between  $L_X$  and  $L_{\text{bol}}$  for these two groups is highly significant<sup>10</sup>. Equal-mass binaries should not contribute to the width of this band, since their shift is expected to be parallel to it (relative to single stars). Neither can X-ray flares be a contributor because we have used quiescent count-rates to derive  $L_X$  (see Sect. 5.1). X-ray variability over longer terms, e.g., days to years, however, might contribute substantially. The spread in the  $L_X$  vs.

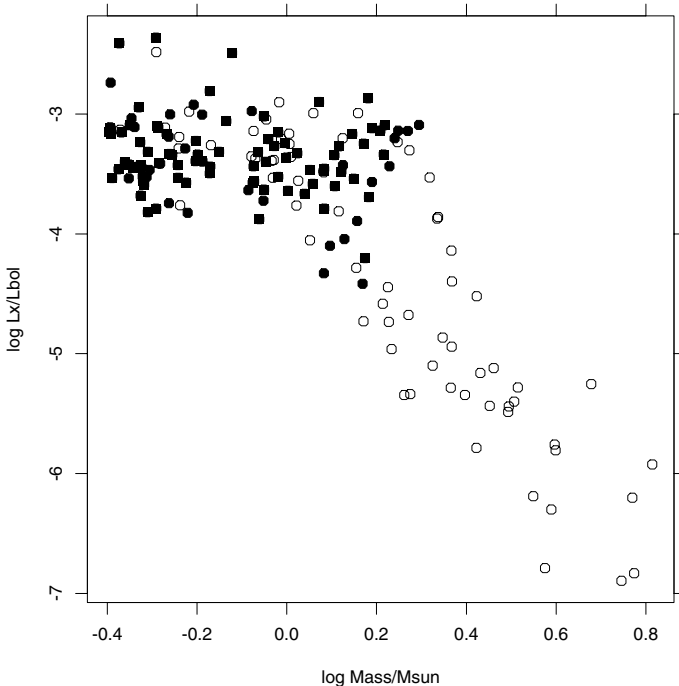
$L_{\text{bol}}$  correlation is 0.33 dex rms (i.e., a factor of 2.2), a rather small value compared to those found in other star-formation regions. The observed spread places an upper bound on possible variation amplitude caused by rotational modulation or long-term cycles like the Sun's, and we thus conclude that in these very young stars, such sources of X-ray variability lead to amplitudes much smaller than the solar range.

Figure 12 shows X-ray luminosity functions for NGC 2362 PMS stars in three mass ranges: 0.5–1  $M_{\odot}$ , 1–2  $M_{\odot}$ , and 2–3  $M_{\odot}$ , using the quiescent X-ray luminosities for flaring X-ray sources. Consistent with our argument that this X-ray sample is complete over these mass ranges, there are no upper limits in the luminosity functions. Stars in the 0.5–1  $M_{\odot}$  mass range have a lower X-ray luminosity function than more massive stars,

<sup>10</sup> Correlation coefficient  $r = 0.6$ ; the probability of this arising from an uncorrelated sample is only  $P < 0.001$ .



**Fig. 12.** X-ray luminosity functions for NGC 2362 PMS stars, in three mass ranges:  $0.5\text{--}1 M_{\odot}$  (solid line),  $1\text{--}2 M_{\odot}$  (dotted line), and  $2\text{--}3 M_{\odot}$  (dashed line).



**Fig. 13.** Ratio of  $L_X$  to  $L_{\text{bol}}$  plotted vs. stellar mass. Symbols same as in Fig. 10.

while stars in the ranges  $1\text{--}2 M_{\odot}$  and  $2\text{--}3 M_{\odot}$  have similar luminosity functions. Comparing the X-ray luminosity functions of NGC 2362 with those of the younger Orion Nebula Cluster (ONC; Flaccomio et al. 2003; Preibisch et al. 2005), we find a small decrease of median X-ray luminosities of NGC 2362 stars with mass  $< 2 M_{\odot}$ , but a much more drastic reduction for stars in the range  $2\text{--}3 M_{\odot}$ . This can be ascribed to the rapid

crossing of these stars in the HR diagram, leading them from K stars with developed convection zones, to A-F stars with shallow or absent convection zones. This agrees well with the older age of NGC 2362 with respect to the Orion Cluster.

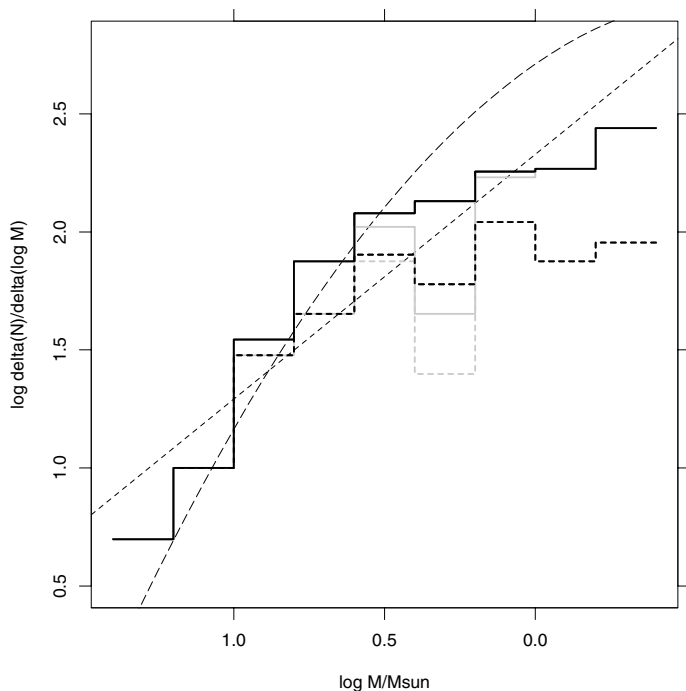
We have explored the question of whether the moderate level of circumstellar activity found for NGC 2362 stars as UV excess or  $H\alpha$  emission could have a detectable impact on X-ray emission. We have compared the X-ray luminosity functions of stars in the most populated mass range  $0.5\text{--}1 M_{\odot}$  with each of these excesses with that of all cluster stars. In all cases, a K-S test yields high probabilities ( $P > 90\%$ ) that these distributions are drawn from the same parent population, implying that the small level of circumstellar activity (accretion) observed in NGC 2362 does not significantly affect coronal emission. This also argues in favor of the completeness of our X-ray selection of NGC 2362 members (down to the limit found above), since there appear to be no X-ray under-luminous stars stemming from strong circumstellar activity (as found for example in Orion, Flaccomio et al. 2003; Preibisch et al. 2005).

Figure 13 is a plot of the ratio  $L_X/L_{\text{bol}}$  vs. stellar mass. For late-type stars (less massive than  $\sim 2 M_{\odot}$ ), the spread in this ratio (from which flare-like variability has been excluded) is small compared, e.g., to the ONC (Flaccomio et al. 2003; Preibisch et al. 2005). The average  $L_X/L_{\text{bol}}$  of low-mass NGC 2362 stars is indicative of “saturated” emission and is very similar to that found for *non-accreting* stars in Orion. A much wider spread (towards lower values) is instead found in Orion, if accreting stars are considered. The narrow  $10^{-3}\text{--}10^{-4}$   $L_X/L_{\text{bol}}$  range should be considered the “canonical” value of *unperturbed* coronae of late-type stars at around 3–5 Myr, while more scattered values can be expected in cases of strong variability (if not excluded in computing  $L_X$ ) or strong accretion of circumstellar material. In NGC 2362, the low fraction of accreting stars and the relative weakness of any accretion (stars with very strong  $H\alpha$  are missing as noted above) implies that even including these accreting stars does not significantly widen the  $L_X/L_{\text{bol}}$  range in Fig. 13.

## 7. The cluster initial mass function

Since we are confident of having selected a reasonably complete sample of cluster stars from the most massive down to stars  $\sim 0.4 M_{\odot}$  ( $V \sim 19$ ), we have attempted to compute the cluster initial mass function (IMF). With this magnitude limit, the use of optical data from the Danish 1.5 m telescope alone eliminates concerns of incomplete spatial coverage in deeper VLT data<sup>11</sup>. A priori, the least complete mass range is expected to be between  $\sim 2\text{--}4 M_{\odot}$ , comprising A-F stars. These stars are typically selected inefficiently in X-ray surveys and could not be selected by different means with available data, since they form no obvious sequence in the HR diagram. The IMF thus derived is shown in Fig. 14 (thick solid line). Note that it flattens considerably towards lower masses ( $\leq 3 M_{\odot}$ ). Exploring further, we have fitted this IMF with a power law (thin short-dashed line in the figure) and found a low index of  $-1.01$ . A flattening towards lower masses is included in some models, such as the log-normal distribution of Chabrier (2003) that includes unresolved binaries and is also shown in Fig. 14 as a thin long-dashed line. In this case too, there is an apparent lack of low-mass stars in our NGC 2362 sample. Our sample selection might have been flawed, however, in several ways: (1) we may have included too many bright stars, some of which could instead be field objects,

<sup>11</sup> The IMF of NGC 2362 at the lowest masses (using these VLT data) was discussed by Moitinho et al. (2005).



**Fig. 14.** The initial mass function of all NGC 2362 stars in the entire ACIS FOV (thick solid line) and in the inner 3' radius (thick dashed line). Grey lines are IMFs computed excluding group #2 stars over the whole ACIS FOV (solid), and over the inner part (dashed). The thin short-dashed line is a power-law fit, while the thin long-dashed line is the Chabrier (2003) model, arbitrarily normalized.

(2) our X-ray selection could be much less complete (e.g., by perhaps a factor  $\sim 2$ – $3$ ) than we argued above or (3) perhaps due to mass segregation, most low-mass stars actually fall outside the ACIS FOV, beyond the region where we computed the IMF.

To examine each of these three possibilities, we make use of the full catalog of Moitinho et al. (2001), which comprises stars outside our ACIS FOV falling over a comparable area and which therefore provides a good comparison. In this comparison sample we find only 2 massive stars (analogues of our group #1 stars), while in the ACIS FOV we find 58, thus ruling out explanation (1).

The low-mass cluster sequence in the HR diagram is very evident, even if we do not mark X-ray sources in it (see e.g. Moitinho et al. 2001 or Dahm 2005), but it disappears entirely if we take away the X-ray sources: it is thus unlikely that there are at least as many X-ray undetected cluster members in this sequence, as there are X-ray detected members. Explanation (2) is therefore not satisfactory.

If we invoke the last possibility, the comparison field should exhibit a cluster sequence of low-mass stars similar to that found in the ACIS FOV, but no such sequence is seen in the HR diagram of the comparison field. This argues that explanation (3) is also unlikely. Such a higher proportion of massive stars with respect to lower-mass stars is also not substantially biased by the inclusion of group #2 stars, whose spread in the HR diagram makes one to suspect a larger contamination by field stars than in other groups: in Fig. 14 we show with grey lines the IMF obtained excluding group #2 stars, which differ appreciably from the previous IMFs only in the range  $\log M/M_{\odot} = 0.2$ – $0.4$  (where they show a little plausible dip), but very little elsewhere. It therefore seems that a real deficit of low-mass stars in NGC 2362, compared to a power law or a log-normal distribution, remains the only viable explanation. This result is similar

to that found by Wilner & Lada (1991) for the same cluster from optical observations down to a limiting magnitude  $I < 17.6$ . (Note however that Kroupa et al. 1992 took exception to Wilner and Lada's result.)

A flattening in the IMF was found in other young clusters (e.g., Orion Trapezium, Muench et al. 2002; Tau-Aur, Briceño et al. 2002; IC 348, Muench et al. 2003), but at lower masses ( $\sim 0.6 M_{\odot}$ ), below which a peak is reached and the IMF starts to decrease. In the case of NGC 2362 such a flattening is probably reached at higher masses, even above  $1 M_{\odot}$ , but down to the lowest masses studied here ( $0.4 M_{\odot}$ ), we do not find a peak and decrease. In agreement with this result, Moitinho et al. (2005) found that the IMF of NGC 2362 starts to decrease for masses below  $0.3 M_{\odot}$  and down to substellar masses.

When we compute the cluster IMF in just the central cluster regions (of diameter 6' or 2.6 pc, thick dashed line in Fig. 14), the result is even flatter, with greater differences from the IMF in other star-forming regions. This stems from mass-segregation effects discussed above. Even this central region, however, is larger than those surveyed in much closer clusters such as IC 348 (Muench et al. 2003 studied  $1.9 \times 1.9$  pc) or the Orion Trapezium (Muench et al. 2002 studied  $0.7 \times 0.7$  pc). This argues that differences between the IMFs of NGC 2362 and other clusters are even larger than indicated here.

## 8. Conclusions

The deeper insights that our new X-ray data have provided into the NGC 2362 stellar population, especially at low masses ( $\leq 2 M_{\odot}$ ), have led to an improved cluster census, now comprising: 226 X-ray selected PMS stars, plus 39  $H\alpha$  selected, X-ray undetected PMS stars, for a total of 265 PMS stars, of which 12 (4.5%) are CTTS as judged by their  $H\alpha$  emission. This falls below the fraction estimated by Dahm (2005) from optical/IR data alone and is also lower than that of stars with circumstellar disks, estimated (from near IR data) by Haisch et al. (2001) to be  $\sim 12\%$ . Since strong  $H\alpha$  emission is generally due to accretion, the fraction of accretion disks (out of all circumstellar disks) is about 0.37, in agreement with the generally accepted picture that not all stars with disks are accreting<sup>12</sup>. If we use UV excesses as an accretion indicator, this fraction approximately doubles but is still compatible with the general picture. We argue that our cluster member sample is likely complete down to  $\sim 0.4 M_{\odot}$ .

The IMF of NGC 2362 is found to be deficient in low-mass stars versus massive stars, as compared with other young clusters. We also find evidence of primordial mass segregation.

In order to corroborate our results, more observational data are needed, both on NGC 2362 itself and on other very young clusters, particularly those without ongoing star formation. Although few such clusters are known (and even fewer are studied in this respect), NGC 6231 or Cyg OB2 may be good examples.

*Acknowledgements.* We thank an anonymous referee for useful comments. We acknowledge support from the Italian MIUR. We also acknowledge a financial contribution from contract ASI-INAF I/023/05/0. We used data from the SIMBAD database, operated at CDS, Strasbourg.

## References

- Argiroffi, C., Maggio, A., Peres, G., Stelzer, B., & Neuhäuser, R. 2005, *A&A*, 439, 1149
- Balona, L. A., & Laney, C. D. 1996, *MNRAS*, 281, 1341

<sup>12</sup> Lada et al. (2005) have recently confirmed this.

- Berghöfer, T. W., & Schmitt, J. H. M. M. 1998, *Cool Stars, Stellar Systems, and the Sun*, ASP Conf. Ser. 154, 2091
- Briceño, C., Luhman, K. L., Hartmann, L., Stauffer, J. R., & Kirkpatrick, J. D. 2002, *ApJ*, 580, 317
- Chabrier, G. 2003, *ApJ*, 586, L133
- Dahm, S. E. 2005, *AJ*, 130, 1805
- Damiani, F., & Micela, G. 1995, *ApJ*, 446, 341
- Damiani, F., Maggio, A., Micela, G., & Sciortino, S. 1997a, *ApJ*, 483, 350
- Damiani, F., Maggio, A., Micela, G., & Sciortino, S. 1997b, *ApJ*, 483, 370
- Damiani, F., Flaccomio, E., Micela, G., et al. 2004, *ApJ*, 608, 781
- Damiani, F., Micela, G., Sciortino, S., et al. 2005, *Star Formation in the Era of Three Great Observatories*
- Damiani, F., Prisinzano, L., Micela, G., & Sciortino, S. 2006, *A&A*, 459, 477
- Dolan, C. J., & Mathieu, R. D. 2001, *AJ*, 121, 2124
- Dolan, C. J., & Mathieu, R. D. 2002, *AJ*, 123, 387
- Flaccomio, E., Damiani, F., Micela, G., et al. 2003, *ApJ*, 582, 398
- Getman, K. V., Flaccomio, E., Broos, P. S., et al. 2005, *ApJS*, 160, 319
- Haisch, K. E., Lada, E. A., & Lada, C. J. 2001, *ApJ*, 553, L153
- Huélamo, N., Stelzer, B., Moitinho, A., Alves, J.F., & Lada, C.J. 2003, *A&SSL*, 299, 194
- Johnson, H. L. 1950, *ApJ*, 112, 240
- Kenyon, S. J., & Hartmann, L. 1995, *ApJS*, 101, 117
- Kroupa, P., Gilmore, G., & Tout, C. A. 1992, *AJ*, 103, 1602
- Lada, C. J., Muench, A. A., Luhman, K. L., et al. 2005, [[arXiv:astro-ph/0511638](https://arxiv.org/abs/astro-ph/0511638)]
- Littlefair, S. P., Naylor, T., Jeffries, R. D., Devey, C. R., & Vine, S. 2003, *MNRAS*, 345, 1205
- Moitinho, A., Alves, J., Huélamo, N., & Lada, C. J. 2001, *ApJ*, 563, L73
- Moitinho, A., Lada, C.J., Huélamo, N., Alves, J.F., & Muench, A. 2005, *A&SSL*, 324, 167
- Muench, A. A., Lada, E. A., Lada, C. J., & Alves, J. 2002, *ApJ*, 573, 366
- Muench, A. A., Lada, E.A.; Lada, C.J., et al. 2003, *AJ*, 125, 2029
- Preibisch, T., Kim, Y.-C.; Favata, F., et al. 2005, *ApJS*, 160, 401
- Raboud, D. 1999, *Rev. Mex. Astron. Astrofis. Conf. Ser.* 8, 107
- Raboud, D., & Mermilliod, J.-C. 1998, *A&A*, 333, 897
- Reid, N., Hawley, S. L., & Mateo, M. 1995, *MNRAS*, 272, 828
- Schmidt-Kaler, Th. 1982, in *Aller, L. H., et al. 1982, Landolt-Bornstein: Numerical Data and Functional Relationships in Science and Technology*
- Siess, L., Dufour, E., & Forestini, M. 2000, *A&A*, 358, 593
- Wheelock, S., et al. 1991, *IRAS Sky Survey Atlas Explanatory Supplement*
- Wilner, D. J., & Lada, C. J. 1991, *AJ*, 102, 1050